

Attosecond time delay during resonance-enhanced multiphoton ionization of Ar in strong laser fields

Xing Li^{1,*}, Xuanhong Gao^{2,*}, Wankai Li¹, Tao Yang¹, Dongdong Zhang¹, Lanhai He^{1,†}, Sizuo Luo¹, Song-Feng Zhao^{2,‡} and Dajun Ding^{1,§}

¹*Institute of Atomic and Molecular Physics, Jilin Provincial Key Laboratory of Applied Atomic and Molecular Spectroscopy, Jilin University, Changchun 130012, China*

²*College of Physics and Electronic Engineering, Northwest Normal University, Key Laboratory of Atomic and Molecular Physics and Functional Materials of Gansu Province, Lanzhou 730070, China*



(Received 17 May 2023; accepted 18 December 2023; published 12 January 2024)

Phase-dependent photoelectron spectra in resonance-enhanced multiphoton ionization (REMPI) of Ar are obtained by scanning the relative phase of two-color femtosecond lasers. Five REMPI channels are resolved and the relative time delays in the attosecond-timescale are extracted. The channel-resolved time delays can be assigned as the contribution of the resonant phase shift of electrons trapped in the specific Rydberg states and also influenced by the phase shift during the continuum-continuum transition. Our observations highlight the important influences of Freeman resonances on photoelectron emission dynamics in strong laser fields and will enable a subfemtosecond photoelectron wavepacket reconstruction in quantum mechanics.

DOI: [10.1103/PhysRevA.109.013103](https://doi.org/10.1103/PhysRevA.109.013103)

I. INTRODUCTION

Photoionization as one of the most fundamental photon-induced processes occurs after photon absorption. The relevant studies promote the development of quantum physics and bring novel insights for physics, chemistry, and materials science [1–6]. Numerous phenomena, e.g., resonance-enhanced multiphoton ionization (REMPI) [7,8], tunneling ionization [9], above-threshold ionization [10,11], photoelectron diffraction [12–14], photoelectron holography [15,16], and strong field autoionization [17,18], have been extensively studied, wherein the real-time electron wavepacket evolution can be traced with attosecond resolution [19,20]. Normally, the experimental observable reveals information on the square of the amplitude of electron wavepackets. However, recent studies accessed the phase of the ionized electron wavepackets, e.g., the group phase delay (Wigner delay) [21,22], benefiting from the advantages of attosecond chronoscopy [19] and ultrafast laser manipulation technologies [23,24]. One way of measuring the phase of a wavepacket is to prepare a well-defined wavepacket and monitor its spatiotemporal interference pattern [25–28]. The relative phase delay, also known as the attosecond time delay of the photoelectron emission, was measured using the techniques of reconstruction of attosecond beating by interference of two-photon transition (RABBITT) [24–26] based on a high-harmonic generation (HHG) sources and a self-calibration exploration with a perturbation from its fundamental frequency pulse. Recently,

this complementary approach was successfully applied to the study of photoionizations during the above-threshold ionization in strong laser fields [29–32], revealing the ultrafast dynamics during photoionization of atoms and molecules within the multiphoton ionization regime. Further development [33] made the probe of the ionization dynamics in the molecular frame possible, thus the angle- and energy-resolved Wigner time delay can be accessed [34].

For instance, a general phenomenon in laser interaction with atoms or molecules is that the excited states would be coupled into the multiphoton resonant channel by Stark effect [35], the so-called Freeman resonance [7]. The time delay between Freeman-resonant ionization has attracted extensive attention. Gong *et al.* observed a 140 as delay between the ionization from $4f$ and $5p$ Rydberg states of the argon atom [31], and confirmed this observation by comparing the results with both the time-dependent Schrödinger equation (TDSE) and generalized quantum trajectory Monte Carlo simulations (GQTM) [36]. Kheifets *et al.* further analyzed the phase difference between the resonant ionization and the direct ionization and found the phase jump of resonant ionization related to the continuum-continuum (CC) transition [37]. While crossing the ionization threshold of noble gas atoms, such as He and Ne, the resonant phase also can be directly measured through the strong RABBITT resonant effects [38] in the $ns \rightarrow np$ transition of lithium atoms, where the infrared (IR) photon energy is close to the energy width of the resonance. Furthermore, the retrapped resonant ionization mechanism [30] was proposed to understand the measured phase delay of near-threshold photoelectrons in the multiphoton ionization of argon atoms. Ge *et al.* studied the angular-dependent relative time delays among the resonant ionization via $4s$, $3d$, and $4f$ states of Ne atoms [8], and found that the time delay also showed strong angular dependence.

*These authors contributed equally to this work.

†helanhai@jlu.edu.cn

‡zhaosf@nwnu.edu.cn

§dajund@jlu.edu.cn

Although the phase-dependent photoelectron yields of multiphoton ionization in a strong laser field (with a $2\omega - \omega$ configuration) were preliminarily explained by the theoretical model [39] recently, the resonant time delay in the multiphoton process is much more complex as multiple paths were involved, and the influence of nonlinear contribution on atomic delays [40] beyond the perturbative regime cannot be ignored, which is structurally different from the traditional RABBITT [25]. Theoretical calculations have predicted [41] that the absorption time delay is nonzero and is proportional to the width of the extreme ultraviolet (XUV) pulse during two-photon resonant ionization. Moreover, the significant time delays could be traced to the retrapped resonant interactions [30] between the ionic Coulomb potential and photoelectron in strong laser fields, which post a new perspective between multiphoton and tunneling regimes in strong-field ionization. Therefore, the detailed analysis of the time delay during multiphoton-resonant ionization in strong laser fields would promote the understanding of photon absorption and develop potentially novel methods for coherent imaging of electron wavepackets.

In this paper, we investigate the relative time delay between different REMPI channels of Ar using phase-stabilized two-color laser fields ($\omega + 2\omega$). Those Freeman-resonant channels (i.e., $3d$, $5p$, $4f$, $5g$, and $6h$ states) are resolved and confirmed from the measured photoelectron spectra. The relative phase delays (time delay) with attosecond temporal resolution for different multiphoton-resonant channels are obtained by scanning the phase delay between two-color laser fields.

II. EXPERIMENTAL AND THEORETICAL METHODS

A. Experimental methods

The REMPI of Ar is investigated by using the interferometric measurement technique. The details were given in our previous papers [32,42–44]. As illustrated in Fig. 1(a), the experimental setup consists of a chirped-pulse amplified (CPA) Ti:sapphire laser system, which provides the fundamental pulse (800 nm, 50 fs, 4 mJ, and 1 kHz), a stable phase-controlled two-color (TC) laser field generator (400 nm + 800 nm), and a velocity map imaging spectrometer (VMIs) [45]. The collinear phase-controlled TC laser beam is produced by an assembly of a β -barium borate (β -BBO) crystal, a calcite crystal, and a pair of fused silica wedges. Briefly, the fundamental (ω , 800 nm) laser beam is introduced into a β -BBO crystal to generate its frequency-doublet pulse (2ω , 400 nm) with the polarization perpendicular to the fundamental pulse. Then, a calcite crystal is used to compensate their relative time delay introduced by the group velocity dispersion of two pulse beams in the entire optical path. The relative phase of TC laser pulses is accurately controlled by moving the fused silica wedges with step of 0.08π (~ 53 as). To perform the strong-field RABBITT experiments in nonresonance and resonance ionization as illustrated in Figs. 1(b) and 1(c), and keep only a single 800-nm photon process involved, the ratio of intensities for the 800-nm and 400-nm laser (set to be about 1:100) is controlled by adjusting the relative angle between the $\lambda/2$ waveplate and the wire grid polarizer, which ensures the polarization directions (y axis) of the two laser

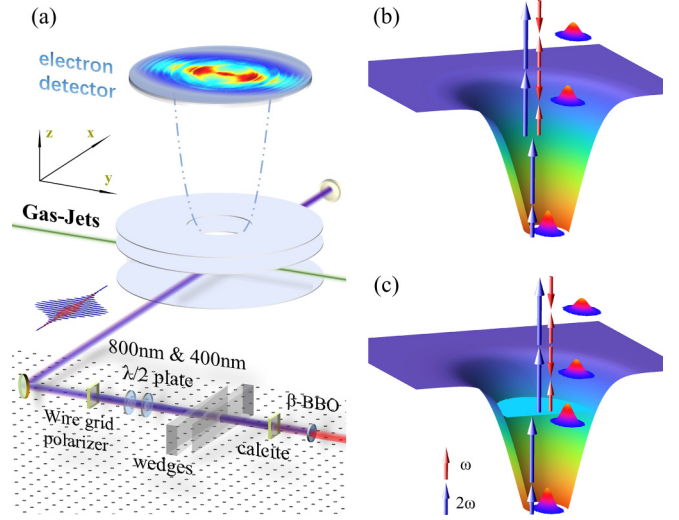


FIG. 1. (a) Schematic illustrations of the experimental setup, (b) the generations of sideband peaks from the photoemission dynamics of main peaks in multiphoton ionization, and (c) resonant ionization via Rydberg states of Ar, by absorbing or emitting an additional photon via the virtual state in the continuum.

pulses are identical. The phase-controlled TC laser beam is focused onto the supersonic Ar gas-jets by a concave mirror ($f = 10$ cm). The generated photoelectrons are guided onto a MCP-phosphor screen assembly by inhomogeneous electric elds in the VMIs. The images of the photoelectron are recorded with a CCD camera and transfer to a computer for further data processing. The iterative Abel inversion method [46] is used to reconstruct the three-dimensional (3D) momentum distribution and extract the energy spectra and photoelectron angular distributions (PADs).

B. Theoretical methods

To simulate experimental photoelectron spectra (PES), we numerically solve the time-dependent Schrödinger equation (TDSE) based on the time-dependent surface flux (tSURFF) method [47].

The laser-atom interaction is described by TDSE with the dipole approximation and the velocity gauge

$$i\partial_t |\Psi(t)\rangle = \hat{H}(t) |\Psi(t)\rangle, \quad (1)$$

where $\hat{H}(t)$ is the Hamiltonian

$$\hat{H}(t) = -\frac{1}{2}\nabla^2 - i\mathbf{A}(t) \cdot \nabla + U(r) - iV_{\text{im}}(r). \quad (2)$$

The vector potential is given by $\mathbf{A}(t) = -\int_0^t \mathbf{E}(t)dt$, the two-color field is written as

$$\mathbf{E}(t) = f(t)[\mathbf{E}_1 \cos(\omega_1 t) + \mathbf{E}_2 \cos(\omega_2 t + \varphi)]. \quad (3)$$

Here, ω_1 (ω_2) is the angular frequency of the 400 (800)-nm laser field and \mathbf{E}_1 (\mathbf{E}_2) is the amplitude of the laser field. A sine-square envelope $f(t)$ of duration $124 T_1$ ($T_1 = 2\pi/\omega_1$) is used; the intensity ratio between polarized laser pulses at 400-nm and 800-nm wavelengths is $I_{400\text{nm}}:I_{800\text{nm}} = 100:1$. $V_{\text{im}}(r)$ is the imaginary potential, which acts as an absorber to exclude unphysical reflections in the wave function outside the numerical bounds, $U(r)$ is the spherically symmetric

potential of atoms, defined as

$$U(r) = \begin{cases} V(r), & r < R_{co}, \\ V'(R_{co})(r - R_{co}) + V(R_{co}), & R_{co} < r < 2R_{co}, \\ 0, & r > 2R_{co}. \end{cases} \quad (4)$$

Here, we use the Tong-Lin potential [48], the analytical form is $V(r) = -(Z_c + a_1 e^{-a_2 r} + a_3 r e^{-a_4 r} + a_5 e^{-a_6 r})/r$, the potential parameters for the argon atom can be found in Ref. [49]. R_{co} is the cutoff radius. When $r > R_{co}$, the potential function is converted to a linear potential, which slope $V'(R_{co})$ is off after reaching zero at $r > 2R_{co}$. Equation (1) can be expanded in terms of the spherical harmonic function. In our numerical simulations, the maximum box size in radial coordinates is $r_{\max} = 2000$ a.u., and the absorbing boundary is $R_{co} = 100$ a.u. The number of partial waves is limited to $L_{\max} = 160$, and the radial coordinate and time steps were 0.01 a.u. and 0.1 a.u., respectively, to ensure convergence of the calculations. The PES amplitudes a_k at time T after the laser pulse is approximated by projecting the part of the wave function that is farther away from the origin than R_l onto Volkov states of the momentum of \mathbf{k} [47]

$$a_{\mathbf{k}} = i \int_0^T dt \langle \chi_{\mathbf{k}}(t) | [\widehat{H}_V, \Theta(r - R_l)] | \Psi(t) \rangle, \quad (5)$$

where $\Theta(r - R_l)$ is the Heaviside step function, $\chi_{\mathbf{k}}(t)$ is the corresponding Volkov wave function, the Volkov wave functions and electron wave function in the region $|r| > R_l$ are evolved by the same nuclear-potential-free Hamiltonian, i.e., $H_V = -\frac{1}{2}\nabla^2 - i\mathbf{A}(t)$. Inserting the time-dependent wave function and the Volkov wave function into Eq. (5) we obtain the following ionization amplitude:

$$a_{\mathbf{k}} = R_l^2 \int_0^T dt \int d\Omega \left\{ \chi_{\mathbf{k}}^*(r, t) \mathbf{A}(t) \Psi(r, t) - \frac{i}{2} [\chi_{\mathbf{k}}^*(r, t) \partial_r \Psi(r, t) - \Psi(r, t) \partial_r \chi_{\mathbf{k}}^*(r, t)] \right\}_{r=R_l}. \quad (6)$$

To avoid an artificial contribution to the time integral, the integrand in Eq. (6) should be multiplied by a Hanning window

$$H(t) = \begin{cases} 1, & \text{if } t < T/2, \\ 1 - [\cos(2\pi t/T)], & \text{if } t \geq T/2. \end{cases} \quad (5)$$

The probability of detecting an electron with the energy $E_{\mathbf{k}}$ in the direction $\theta_{\mathbf{k}}$

$$P(E_{\mathbf{k}}, \theta_{\mathbf{k}}) = 2\pi k |a_{\mathbf{k}}|^2 \quad (8)$$

and then PES is given by

$$dP/dE_{\mathbf{k}} = \int_0^{\theta_{\mathbf{k}}} 2\pi \mathbf{k} \sin(\theta_{\mathbf{k}}) |a_{\mathbf{k}}|^2 d\theta_{\mathbf{k}}. \quad (9)$$

III. RESULT AND DISCUSSIONS

The measured photoelectron distributions from strong-field ionization of Ar at single color (400 nm) and TC lasers (400 nm + 800 nm) are shown in Figs. 2(a) and 2(b). The intensity of the 400-nm laser pulse is chosen to produce resolvable ATIs via REMPI through a series of Rydberg states.

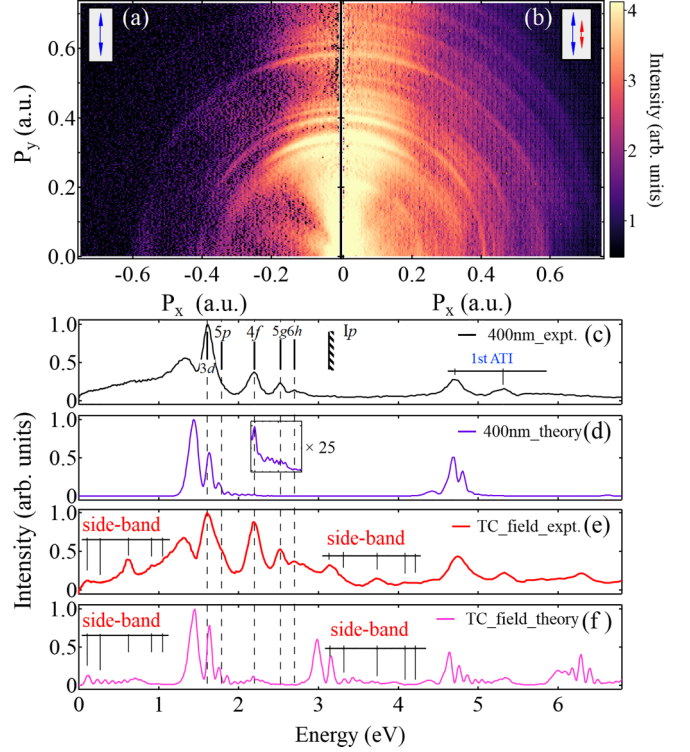


FIG. 2. Contrast diagram of the measured photoelectron momentum in the detector plane for (a) 400-nm field (b) TC field (integrated over 2π phase). [(c)–(f)] The measured and calculated photoelectron spectra at the single 400-nm field and the TC field, respectively.

In this work, it is 1.0×10^{14} W/cm² and 1.4×10^{14} W/cm², which will be referred to as low intensity and high intensity, respectively, in the following. While the intensity of 800 nm used is weak enough to ensure one photon transition for producing the sideband channels. The well-resolved photoelectron distributions contributed from REMPI are shown in Fig. 2(a), and the sideband structures can be clearly seen in Fig. 2(b) when a weak 800 nm is added. For further comparing the REMPI process of Ar at these two laser conditions, the corresponding photoelectron kinetic energy distributions are given in Figs. 2(c) and 2(e). After absorbing 400-nm photons, the ground state may be ionized through either a direct six-photon (the peak centred around 1.3 eV) or resonant-enhanced MPI with a certain Rydberg states dressed by the laser field through the Stark effect. The assignments of those resonance channels are labeled in Fig. 2(c) [50,51]. The theory reconstructs the peak positions of these REMPI channels observed in the experiment, while the relative yields do not agree quantitatively. This discrepancy arises from the narrow bandwidth of a 60-fs laser pulse used in simulations considering the computational costs, making it challenging to satisfy the resonance conditions and leading to relatively low yields of resonance peaks [52]. Furthermore, the laser parameters used in the simulations are not precisely matched to the real experiment due to the laser intensity uncertainties and volume effect, which would also lead to low yields of the high Rydberg state in the theory. Even though there is a clear difference in the amplitudes for the measured and simulated PES, this discrepancy would not affect the relative phase analysis, as

the dependence of the amplitudes does not affect the phase of the oscillation [53].

As illustrated in Fig. 1(c), the first-order sideband arises from the interference of two paths, one is the absorption of a single 800-nm photon, and the other is the release of an 800-nm photon after absorbing a single 400-nm photon. This is consistent with the model of underthreshold RABBITT recently proposed by Kheifets [37]. In Fig. 2(e), the main REMPI channels and the corresponding sidebands are marked with the same color text. The population of multiple Rydberg states in one measurement offers us a unique opportunity to measure the relative ionization time delay between these REMPI channels. The high-intensity result looks similar to the low-intensity one and is not shown here.

We measured the ionization time delay of Ar with the similar experimental protocol of Zipp *et al.* [29] by scanning the relative phase delay between the 400-nm and 800-nm lasers, in analogy to the scheme of two-channel interference in the RABBITT measurement [25]. The signal magnitude of the q th photoelectron peak oscillates with the relative time delay τ between TC laser fields and takes the form [25,29]

$$S^q = A_0 + B_0 \cos(2\omega\tau + \varphi). \quad (10)$$

Here, the φ can be further written as

$$\varphi = \varphi_{\text{pump}} + \varphi_{\text{atom}} + \varphi_{\text{cc}}, \quad (11)$$

in which the φ_{pump} is the accumulated phase delay during multiphoton absorption by the pump laser. φ_{atom} is the intrinsic phase delay in the process of atomic photoionization. φ_{cc} is known as the phase delay during the continuum-continuum transition. The time delay can be calculated by $\tau_l = \varphi/(2\omega)$.

Here, we first compare and analyze the measured phase delay (ionization time delay) of nonresonance ionization, i.e., multiphoton ionization, before diagnosing the ionization delay in REMPI. Figures 3(a) and 3(b) show the phase-integrated photoelectron spectra for the experiment and simulation in the high laser intensity, and there is also a well-resolved ATI comb with energy difference equal to 1.55 eV (one 800-nm photon) in the spectra. It is noteworthy that the measured phase dependence of the ATI and sideband show a similar behavior as previously reported [8,54]. The ATIs and sidebands present distinguished oscillations with a phase difference around π . As shown in Fig. 3(c), we set the time delay of the fourth sideband (12.2 eV) to zero in these two separate measurements as a reference point. At low laser intensity (similar to the laser condition used by Zipp *et al.*), the measured time delay for ATIs and sidebands agree with previous results [29,31] in which the time delay for electrons with the energy above 5 eV is zero roughly for sidebands, which was proved by the TDSE and GQTMC calculations [30]. Notably, the delay time decreases from 100 as to 0 as when the electron energy increases from 2.9 eV to 13 eV for the measured sidebands, which suggests the Coulomb distortion effect has an important contribution for the electrons with low final energy and the influence becomes weaker as the photoelectron energy increases. Furthermore, the oscillation of the main ATI is out of $\sim\pi$ phase with the sideband peaks at high energy, which is consistent with the theoretical prediction of strong-field RABBITT [55]. Different from the strong-field approximation (SFA) theory that the phase shift between ATI and SB tends

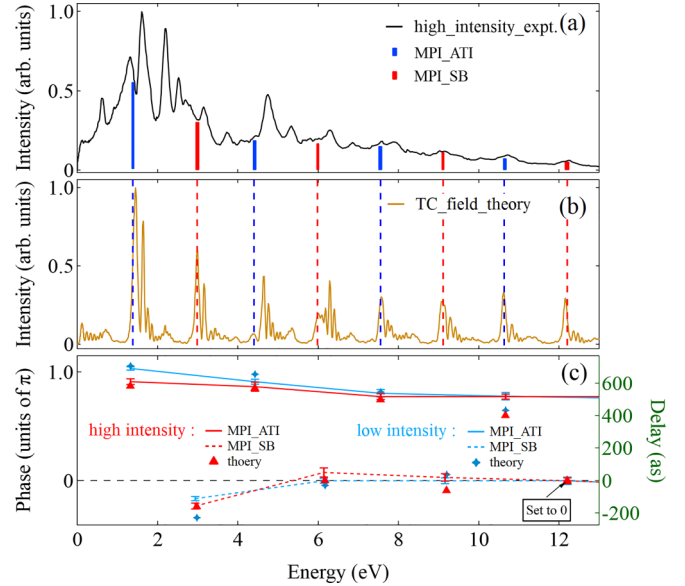


FIG. 3. The (a) measured and (b) simulated photoelectron spectra in the TC laser field with high intensity. (c) The phase results in comparison between the experiment and TDSE simulation. For the experiments, low- and high-intensity results are shown as blue (light gray) and red (gray) lines, and for the theory blue asterisks and red triangles, respectively. The error bars are derived from the experimental standard deviation of the phase parameter fitting of the integrated energy peak oscillation asymmetry.

to π at higher electron energies, López's work [39] shows that the coupling of Coulomb field and laser field, and the influence of the laser field intensity changing on the phase delay cannot be ignored, resulting in an offset between the sidebands and ATI (less than π). The energy-dependent phase delay of ATIs and sidebands in our work also shows a similar tendency. However, some differences between experimental and theoretical results in the lower-energy region also indicate the profound complexity of strong-field ionization. This may be induced by the effect of laser Coulomb coupling or high-order transition interference during the multiphoton ionization [28,55].

The phase-dependent ATIs and their sideband signals indicate that our measurement is reliable for tracking the ionization time delay of electrons with attosecond precision. Now, we discuss the REMPI channels. Figures 4(b) and 4(c) give the measured and simulated phase-dependent photoelectron spectra at the high laser intensities. Five Rydberg states involved in REMPI are observed and assigned in the spectra as shown in Fig. 4(a) within the energy range below 7 eV. Taking the first-order sideband originating from ionization of the $3d$ state as an example, the pathway is assigned as follows: the Ar is excited to a $3d$ state by absorbing five 400-nm photons, and then two ionization channels occur with one absorbing an 800-nm photon leading to ionization, and the other absorbing one 400-nm photon first and emitting one 800-nm photon. The electrons generated from these two channels reach the same final energy (0.08 eV) and interfere. The result of our TDSE model well reproduced our measurements.

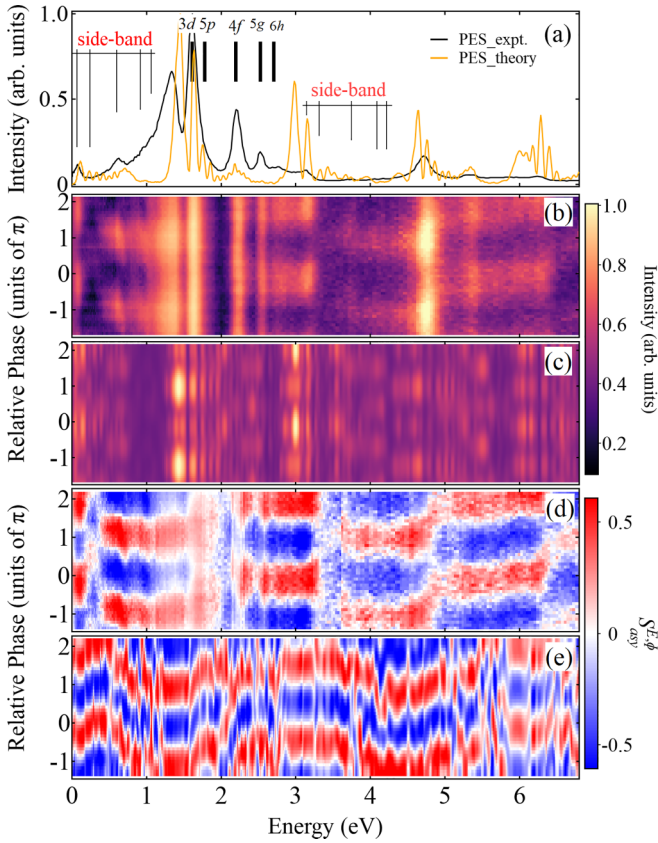


FIG. 4. Phase-integrated photoelectron energy distribution of the (b) experiment and (c) TDSE simulation in the energy region below 7 eV with black (gray) and orange (light gray), respectively. Corresponding phase-integrated photoelectron spectra as theory and experiment are shown in (a) with orange (light gray) and black (gray) lines, respectively. The asymmetry $S_{asy}^{E,\phi}$ parameter for the (d) experiment and (e) simulation.

We further calculate the asymmetry parameters as $S_{asy}^{E,\phi} = (S_{up}^{E,\phi} - S_{down}^{E,\phi}) / (S_{up}^{E,\phi} + S_{down}^{E,\phi})$ to refine the phase-dependent sidebands' oscillation for REMPI phases, and the asymmetry parameters can effectively eliminate the measurement uncertainty introduced by the experimental system such as the insufficient laser intensity stability, where the $S_{up,down}^{E,\phi}$ is the measured angle-integrated electron yield of emission spectra in the up- and down-side of the detector, respectively. The measured and simulated phase-dependent asymmetry parameters are shown in Figs. 4(d) and 4(e). Then the signals can be fitted by Eq. (10). For the theory, the ionization phase was retrieved from the first term of the Fourier transform [39]. The obtained energy-dependent delay time of electrons from sidebands of these REMPI channels are shown in Fig. 5. As a confirmatory comparison, upon applying a 2π folding to the phase of the $5p$ peak, the retrieved time delay between $4f$ and $5p$ of $\Delta\tau_{4f-5p}^1 = 147$ as in the high intensity is consistent with that obtained through the orthogonal two-color laser field [31]. Moreover, the large relative time delays also exist between $3d$ and $4f$ states, $\Delta\tau_{3d-4f}^1 = 460$ as, while the relative time delay of $5g$ and $6h$ with respect to $4f$ are small. Our measurements indicate that the relative delays between different REMPI channels are sensitive to the corresponding Rydberg states, but

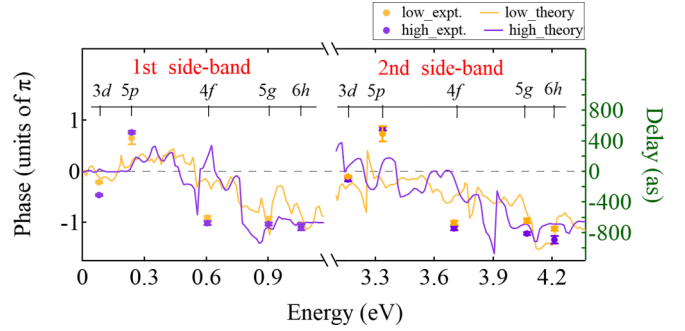


FIG. 5. The first- and second-order retrieved phase for the observed peaks of resonant states sidebands as a function of the energy of photoelectron for different REMPI channels. Low- and high-intensity results are shown in orange (light gray) and purple (gray) for experiment and theory, respectively.

have a very weak dependence on the intensities of the pump laser, while noting that the interpretation of such experiments is more complicated than in the typical RABBITT [25,56] framework.

The observed phase delay can be described by Eq. (11), wherein φ_{pump} can be eliminated while comparing the relative delay between channels absorbing the same number of photons. The atomic phase φ_{atom} is the group delay when the liberated photoelectron passes the Coulomb potential, i.e., the Wigner delay. Specifically, the resonant phase φ_{res} would additionally enlarge the φ_{atom} during the REMPI process. Normally, the Wigner delay decreases as the energy of the electron increases, and the Wigner delay becomes very small when the energy of the electron is high enough for the direct ATI electrons. The resonant phase shift can be written as [37] $\varphi_{res} = \arctan(\Gamma/\Delta)$, where Γ is the spectra width and Δ is the detuning induced by the external field. In this case, the relative delay time during the REMPI is also affected by the laser intensities or central IR frequency ω [37,38]. The effect of φ_{pump} can be visualized and further confirmed by comparing the measured delay times at different pump laser intensities, as shown in Fig. 5. Furthermore, changing the intensities of the pump laser would also detune the resonance, which will lead to a phase shift. The last term φ_{cc} , i.e., the delays from the continuum-continuum transition, also depends on the energy of the photoelectron [25]. In general, φ_{cc} can be ignored for ionization channels with similar kinetic energies [32] or on the relatively high kinetic energy regime [57]. For the case of near-threshold ionization, the effect of φ_{cc} becomes significant [37].

The energy dependence of the relative time delay φ_{wigner} and φ_{cc} can be discussed by comparing the relative time delay among the sidebands of different REMPI channels. Figure 5 shows the evolution of the relative delays of these different REMPI channels under two laser intensities, which show similar behavior. Our observations for the delays of different REMPI channels on the two-order sidebands cannot be simply explained by the contribution of φ_{wigner} and φ_{cc} because these two delays of the first- and second-order sideband show similar trends with the energy of the electron. The phase jump near the threshold between resonant and nonresonant ionization is explained with lowest-order perturbation theory [37],

which may not be suitable for explaining the measured delay time in a strong laser field, especially for the second-order sideband that does not satisfy the model [58]. In addition, some subtle phase differences were observed between low and high intensities. We speculate this might be caused by the modifications of detuning through the laser-field-induced Stark effect. However, an unambiguous analysis would demand further experimental and theoretical investigations.

Therefore, the measured relative delay time can be assigned as the contribution of the resonant phase shift of electrons trapped in the bound Rydberg states and also influenced by the phase shift during the continuum-continuum transition. It is clear that the time delays in both resonant ionization channels are not uniform, the produced electron would stay on the resonant intermediate states for a significant time before transitioning to the continuum [8,30]. The measured different phase points may be influenced by several related factors, such as the number of photons absorbed or the angular momentum of the Rydberg electron [59], all of these things may contribute to the time delays between the resonant states.

IV. CONCLUSION

In summary, we studied the relative time delay of REMPI channels during strong field ionization of Ar with ultrafast phase-controlled photoelectron spectroscopy. The attosecond

delay time between five Rydberg states ($3d$, $5p$, $4f$, $5g$, and $6h$) are extracted by scanning the relative phase of 400-nm and 800-nm lasers. The different contributions of phase components, i.e., φ_{laser} , φ_{pump} , φ_{res} , and φ_{cc} , are discussed based on the observed channel- and order-resolved delay times during REMPI. The channel-resolved time delays can be assigned as the contribution of the resonant phase shift of electrons trapped in the specific Rydberg states and also influenced by the phase shift during the continuum-continuum transition. Even though the time delay during REMPI can be precisely obtained from the measurements and reproduced by the TDSE model, the physical mechanisms to comprehensively explain the ionization time delay during REMPI remain challenging because of the large number of electronic states involved and the complicated electronic many-body effects. Nevertheless, this work will promote the understanding of photon absorption and bring additional information on the multiphoton ionization of atoms and molecules. Our findings provide a reference for building a more complete theoretical description, which we are looking for.

ACKNOWLEDGMENT

This work was supported by the National Natural Science Foundation of China (Grants No. 12134005, No. 12164044, No. 92250306, and No. 11704147).

-
- [1] F. Krausz and M. Ivanov, *Rev. Mod. Phys.* **81**, 163 (2009).
 - [2] F. Lépine, M. Y. Ivanov, and M. J. J. Vrakking, *Nat. Photon.* **8**, 195 (2014).
 - [3] A. L. Cavalieri, N. Müller, T. Uphues, V. S. Yakovlev, A. Baltuška, B. Horvath, B. Schmidt, L. Blümel, R. Holzwarth, S. Hendel, M. Drescher, U. Kleineberg, P. M. Echenique, R. Kienberger, F. Krausz, and U. Heinzmann, *Nature (London)* **449**, 1029 (2007).
 - [4] M. Schultze, E. M. Bothschafter, A. Sommer, S. Holzner, W. Schweinberger, M. Fiess, M. Hofstetter, R. Kienberger, V. Apalkov, V. S. Yakovlev, M. I. Stockman, and F. Krausz, *Nature (London)* **493**, 75 (2013).
 - [5] M. Schultze, K. Ramasesha, C. Pemmaraju, S. Sato, D. Whitmore, A. Gandman, J. S. Prell, L. J. Borja, D. Prendergast, K. Yabana, D. M. Neumark, and S. R. Leone, *Science* **346**, 1348 (2014).
 - [6] A. Sommer, E. M. Bothschafter, S. A. Sato, C. Jakubeit, T. Latka, O. Razskazovskaya, H. Fattahi, M. Jobst, W. Schweinberger, V. Shirvanyan, V. S. Yakovlev, R. Kienberger, K. Yabana, N. Karpowicz, M. Schultze, and F. Krausz, *Nature (London)* **534**, 86 (2016).
 - [7] R. R. Freeman, P. H. Bucksbaum, H. Milchberg, S. Darack, D. Schumacher, and M. E. Geusic, *Phys. Rev. Lett.* **59**, 1092 (1987).
 - [8] P. Ge, M. Han, M.-M. Liu, Q. Gong, and Y. Liu, *Phys. Rev. A* **98**, 013409 (2018).
 - [9] P. Eckle, A. N. Pfeiffer, C. Cirelli, A. Staudte, R. Dörner, H. G. Muller, M. Büttiker, and U. Keller, *Science* **322**, 1525 (2008).
 - [10] M. Busuladžić, A. Gazibegović-Busuladžić, D. B. Milošević, and W. Becker, *Phys. Rev. Lett.* **100**, 203003 (2008).
 - [11] C. Liu, T. Nakajima, T. Sakka, and H. Ohgaki, *Phys. Rev. A* **77**, 043411 (2008).
 - [12] T. Zuo, A. D. Bandrauk, and P. B. Corkum, *Chem. Phys. Lett.* **259**, 313 (1996).
 - [13] M. Meckel, D. Comtois, D. Zeidler, A. Staudte, D. Pavii, H. C. Bandulet, H. Pépin, J. C. Kieffer, R. Dörner, D. M. Villeneuve, and P. B. Corkum, *Science* **320**, 1478 (2008).
 - [14] C. Wang, M. Okunishi, R. R. Lucchese, T. Morishita, O. I. Tolstikhin, L. B. Madsen, K. Shimada, D. Ding, and K. Ueda, *J. Phys. B: At. Mol. Opt. Phys.* **45**, 131001 (2012).
 - [15] Y. Huismans, A. Rouzée, A. Gijsbertsen, J. H. Jungmann, A. S. Smolkowska, P. S. W. M. Logman, F. Lépine, C. Cauchy, S. Zamith, T. Marchenko *et al.*, *Science* **331**, 61 (2011).
 - [16] X.-B. Bian, Y. Huismans, O. Smirnova, K.-J. Yuan, M. J. J. Vrakking, and A. D. Bandrauk, *Phys. Rev. A* **84**, 043420 (2011).
 - [17] U. Fano, *Phys. Rev.* **124**, 1866 (1961).
 - [18] S. Luo, J. Liu, X. Li, D. Zhang, X. Yu, D. Ren, M. Li, Y. Yang, Z. Wang, P. Ma, C. Wang, J. Zhao, Z. Zhao, and D. Ding, *Phys. Rev. Lett.* **126**, 103202 (2021).
 - [19] R. Pazourek, S. Nagele, and J. Burgdörfer, *Rev. Mod. Phys.* **87**, 765 (2015).
 - [20] J. M. Dahlström, D. Guénot, K. Klünder, M. Gisselbrecht, J. Mauritsson, A. L. Huillier, A. Maquet, and R. Taïeb, *Chem. Phys.* **414**, 53 (2013).
 - [21] E. P. Wigner, *Phys. Rev.* **98**, 145 (1955).
 - [22] F. T. Smith, *Phys. Rev.* **118**, 349 (1960).
 - [23] S. Nagele, R. Pazourek, J. Feist, K. Doblhoff-Dier, C. Lemell, K. Tőkési, and J. Burgdörfer, *J. Phys. B: At. Mol. Opt. Phys.* **44**, 081001 (2011).

- [24] P. M. Paul, E. S. Toma, P. Breger, G. Mullot, F. Augé, P. Balcou, H. G. Muller, and P. Agostini, *Science* **292**, 1689 (2001).
- [25] K. Klünder, J. M. Dahlström, M. Gisselbrecht, T. Fordell, M. Swoboda, D. Guénot, P. Johnsson, J. Caillat, J. Mauritsson, A. Maquet, R. Taïeb, and A. L'Huillier, *Phys. Rev. Lett.* **106**, 143002 (2011).
- [26] J. M. Dahlström, A. L'Huillier, and A. Maquet, *J. Phys. B: At. Mol. Opt. Phys.* **45**, 183001 (2012).
- [27] H. G. Muller, *Appl. Phys. B* **74**, s17 (2002).
- [28] M. Isinger, R. J. Squibb, D. Busto, S. Zhong, A. Harth, D. Kroon, S. Nandi, C. L. Arnold, M. Miranda, J. M. Dahlström, E. Lindroth, R. Feifel, M. Gisselbrecht, and A. L'Huillier, *Science* **358**, 893 (2017).
- [29] L. J. Zipp, A. Natan, and P. H. Bucksbaum, *Optica* **1**, 361 (2014).
- [30] X. Song, G. Shi, G. Zhang, J. Xu, C. Lin, J. Chen, and W. Yang, *Phys. Rev. Lett.* **121**, 103201 (2018).
- [31] X. Gong, C. Lin, F. He, Q. Song, K. Lin, Q. Ji, W. Zhang, J. Ma, P. Lu, Y. Liu, H. Zeng, W. Yang, and J. Wu, *Phys. Rev. Lett.* **118**, 143203 (2017).
- [32] X. Li, Y. Liu, D. Zhang, L. He, S. Luo, C.-C. Shu, and D. Ding, *Phys. Rev. A* **108**, 023114 (2023).
- [33] S. Eckart, *Phys. Rev. Res.* **2**, 033248 (2020).
- [34] D. Trabert, S. Brennecke, K. Fehre, N. Anders, A. Geyer, S. Grundmann, M. S. Schöffler, L. P. H. Schmidt, T. Jahnke, R. Dörner, M. Kunitski, and S. Eckart, *Nat. Commun.* **12**, 1697 (2021).
- [35] P. Agostini, P. Breger, A. L'Huillier, H. G. Muller, G. Petite, A. Antonetti, and A. Migus, *Phys. Rev. Lett.* **63**, 2208 (1989).
- [36] X. Song, C. Lin, Z. Sheng, P. Liu, Z. Chen, W. Yang, S. Hu, C. D. Lin, and J. Chen, *Sci. Rep.* **6**, 28392 (2016).
- [37] A. S. Kheifets and A. W. Bray, *Phys. Rev. A* **103**, L011101 (2021).
- [38] A. S. Kheifets, *Phys. Rev. A* **104**, L021103 (2021).
- [39] S. D. López, S. Donsa, S. Nagele, D. G. Arbó, and J. Burgdörfer, *Phys. Rev. A* **104**, 043113 (2021).
- [40] D. G. Arbó, S. D. López, and J. Burgdörfer, *Phys. Rev. A* **106**, 053101 (2022).
- [41] J. Su, H. Ni, A. Jaroń-Becker, and A. Becker, *Phys. Rev. Lett.* **113**, 263002 (2014).
- [42] W. Hu, X. Li, H. Zhao, W. Li, Y. Lei, X. Kong, A. Liu, S. Luo, and D. Ding, *J. Phys. B: At. Mol. Opt. Phys.* **53**, 084002 (2020).
- [43] W. Hu, Y. Liu, S. Luo, X. Li, J. Yu, X. Li, Z. Sun, K.-J. Yuan, A. D. Bandrauk, and D. Ding, *Phys. Rev. A* **99**, 011402(R) (2019).
- [44] Y. Liu, W. Hu, S. Luo, K.-J. Yuan, Z. Sun, A. D. Bandrauk, and D. Ding, *Phys. Rev. A* **100**, 023404 (2019).
- [45] A. T. J. B. Eppink and D. H. Parker, *Rev. Sci. Instrum.* **68**, 3477 (1997).
- [46] M. J. J. Vrakking, *Rev. Sci. Instrum.* **72**, 4084 (2001).
- [47] V. Tulsy and D. Bauer, *Comput. Phys. Commun.* **251**, 107098 (2020).
- [48] X. M. Tong and C. D. Lin, *J. Phys. B: At. Mol. Opt. Phys.* **38**, 2593 (2005).
- [49] S.-F. Zhao, N. Wang, Y.-J. Li, Z. Guan, G.-L. Wang, T. Morishita, and P.-C. Li, *J. Phys. B: At. Mol. Opt. Phys.* **54**, 175601 (2021).
- [50] C. M. Maharjan, A. S. Alnaser, I. Litvinyuk, P. Ranitovic, and C. L. Cocke, *J. Phys. B: At. Mol. Opt. Phys.* **39**, 1955 (2006).
- [51] R. Wiehle, B. Witzel, H. Helm, and E. Cormier, *Phys. Rev. A* **67**, 063405 (2003).
- [52] D. Chetty, R. D. Glover, B. A. deHarak, X. M. Tong, H. Xu, T. Pauly, N. Smith, K. R. Hamilton, K. Bartschat, J. P. Ziegel, N. Douguet, A. N. Luiten, P. S. Light, I. V. Litvinyuk, and R. T. Sang, *Phys. Rev. A* **101**, 053402 (2020).
- [53] M. Isinger, D. Busto, S. Mikaelsson, S. Zhong, C. Guo, P. Salières, C. L. Arnold, A. L'Huillier, and M. Gisselbrecht, *Philos. Trans. R. Soc. A* **377**, 20170475 (2019).
- [54] Y. Feng, M. Li, S. Luo, K. Liu, B. Du, Y. Zhou, and P. Lu, *Phys. Rev. A* **100**, 063411 (2019).
- [55] M. Bertolino and J. M. Dahlström, *Phys. Rev. Res.* **3**, 013270 (2021).
- [56] M. Huppert, I. Jordan, D. Baykusheva, A. von Conta, and H. J. Wörner, *Phys. Rev. Lett.* **117**, 093001 (2016).
- [57] S. Nandi, E. Plésiat, S. Zhong, A. Palacios, D. Busto, M. Isinger, L. Neorii, C. L. Arnold, R. J. Squibb, R. Feifel, P. Declava, A. L. Huillier, F. Martín, and M. Gisselbrecht, *Sci. Adv.* **6**, eaba7762 (2020).
- [58] D. Bharti, D. Atri-Schuller, G. Menning, K. R. Hamilton, R. Moshhammer, T. Pfeifer, N. Douguet, K. Bartschat, and A. Harth, *Phys. Rev. A* **103**, 022834 (2021).
- [59] X. Yu, N. Wang, J.-T. Lei, J.-X. Shao, T. Morishita, S.-F. Zhao, B. Najjari, X.-W. Ma, and S.-F. Zhang, *Phys. Rev. A* **106**, 023114 (2022).